Article
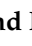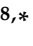
Vapor Barrier Properties of Cold Plasma Treated Corn Starch Films

Marta D. da Fonseca de Albuquerque [1], Daniele C. Bastos [2], Ştefan Ţălu [3,*], Robert S. Matos [4], Marcelo A. Pires [5], Marco Salerno [6], Henrique D. da Fonseca Filho [7] and Renata A. Simão [8,*]

1 Laboratory for Surface Chemistry, Coordination of Process and Mineral Technologies, Centre for Mineral Technology—CETEM, Av. Pedro Calmon 900, Ilha da Cidade Universitária, Rio de Janeiro 21941-908, RJ, Brazil; mduarte@cetem.gov.br

2 Department of Materials, State University of Rio de Janeiro—UERJ-ZO, Avenida Manuel Caldeira de Alvarenga 1203, Campo Grande, Rio de Janeiro 23070-200, RJ, Brazil; daniele_cruz@yahoo.com.br

3 The Directorate of Research, Development and Innovation Management (DMCDI), Technical University of Cluj-Napoca, Constantin Daicoviciu St., No. 15, 400020 Cluj-Napoca, Romania

4 Postgraduate Program in Materials Science and Engineering, Federal University of Sergipe, São Cristóvão 49100-000, SE, Brazil; amazonianmaterialsgroup@gmail.com

5 Department of Physics, Federal University of Ceará—UFC, Fortaleza 60180-020, CE, Brazil; pires.ma.fisica@gmail.com

6 Institute for Globally Distributed Open Research and Education (IGDORE), and Institute for Materials Science and Max Bergmann Center of Biomaterials, Technische Universität Dresden, 01069 Dresden, Germany; marco.salerno@igdore.org

7 Laboratory of Synthesis of Nanomaterials and Nanoscopy, Physics Department, Federal University of Amazonas—UFAM, Manaus 69067-005, AM, Brazil; hdffilho@ufam.edu.br

8 Metallurgical and Materials Engineering Program—PEMM/COPPE, Federal University of Rio de Janeiro, Ilha da Cidade Universitária, Rio de Janeiro 21941-972, RJ, Brazil

* Correspondence: stefan_ta@yahoo.com or stefan.talu@auto.utcluj.ro (Ş.Ţ.); renata@metalmat.ufrj.br (R.A.S.)

Abstract: The development and efficient production of effective bioplastics is a hot topic, required to face up to the issue of the difficult disposal of plastics derived from oil. Among the different natural sources of bioplastics, starch is one of the most promising. However, for most applications, the proper mastering of the surface properties of bioplastic is necessary. We report about the surface modification of extruded corn starch films by means of cold plasma based on helium (He) and hexamethyldisiloxane (HMDSO). The differently treated surfaces were functionally characterized in wettability and water absorption. The nanoscale morphology was assessed by scanning electron microscopy and atomic force microscopy. The obtained images were analyzed by advanced figures describing both texture and amplitude parameters, including fractal behavior. The combined treatment (He/HMDSO) resulted in more homogeneous films with smaller, better-distributed grains compared to the case wherein He was not used. Despite the different morphologies observed, starch coated by HMDSO alone and by He/HMDSO presented similar hydrophobic character, with contact angles higher than 110°. Plasma treatment with HMDSO and He/HMDSO resulted in a significant reduction of absorbed water content without reduction of water vapor permeability. The nanotexture of the films did not present statistically significant differences, in terms of spatial complexities, dominant spatial frequencies, homogeneous void distribution, and surface percolation.

Keywords: atomic force microscopy; cold plasma; plasma coatings; helium; hexamethyldisiloxane; nanostructures; starch; surface morphology

1. Introduction

Problems caused by the disposal of synthetic plastics made from petroleum are prompting the development of environmentally compatible materials derived from renewable sources [1–3]. In recent years, there has been great interest in the development of natural thermoplastic materials mainly composed of starch [4,5], since this polymer has low

production cost and excellent biodegradability and is available from abundant renewable sources [6,7]. However, starch-based plastics are highly susceptible to water absorption because of their hydrophilicity, limiting their applications. Water absorption can result in the loss of a material's mechanical and barrier properties [8–10].

Cold plasma technology has been widely used to modify the surface of polymeric materials, mainly because it is a clean method that does not alter the bulk properties of the material [11–13]. An inert gas plasma, such as helium or argon, is generally used for pretreatment to clean substrates before the application of reactive gases [14]. Treatment with hexamethyldisiloxane (HMDSO) plasma can be used, in turn, to provide the materials with a hydrophobic coating or corrosion protection layer, to make barrier films for food packaging and pharmaceutical products, among other applications [15–17]. To modify starch film surfaces, Bastos et al. [6] employed a surface-modification method based on two precursor gases, HMDSO and SF_6, and combined treatments using HMDSO followed by SF_6 (HMDSO/SF_6) and the reverse order (SF_6/HMDSO). The results indicated that the induced surface morphology determined the contact angle. It was reported that all films became hydrophobic and that films initially treated with SF_6 showed the greatest hydrophobicity when no further coating was applied or when the treated surface was further coated using HMDSO. Under both treatment conditions, the contact angle was greater than 110°. Albuquerque et al. [18] compared helium (He) plasma treatment and HMDSO plasma coating as different means for the hydrophobization of thermoplastic starch (TPS) surfaces obtained by casting. The TPS surfaces were treated with He plasma, He plasma followed by HMDSO, and HMDSO plasma alone. The results indicated that He plasma treatment was not able to induce changes in surface wettability, but HMDSO coating led to surface hydrophobization, both in as-prepared starch films and the He-modified surfaces.

As for many other technological materials, the morphology of the starch films characterized here can be of critical importance in view of its consequences on the chemical and physical functional properties of the respective surface. It is well-known that the best tool for assessing this 3D surface morphology directly in real space and in reliable manner is the atomic force microscope (AFM). Following raw-data collection by AFM, the next step for deeper understanding is advanced image analysis. Among the many parameters used in the past to accurately describe the 3D surface properties are height-distribution figures [19–24], power spectrum density [23,25,26], and fractal [27–29] and multifractal figures [30–32]. These methods of advanced image analysis have also recently been applied to investigating the surface of films based on polymeric macromolecules [21,33–36].

In this study, extruded TPS films were modified by plasma in two different ways: (i) using a reactive gas (HMDSO) as precursor and (ii) using a non-reactive gas (He) followed by HMDSO (He/HMDSO) as precursors. The film surfaces were characterized before and after the plasma treatment by scanning electron microscopy (SEM), AFM, contact angle measurement, water vapor permeation (WVP) testing, and water absorption testing. We hypothesize that hydrophobic coatings are a barrier for water vapor permeation and that both surface wettability and water vapor permeation are affected by surface morphology.

2. Material and Methods

2.1. Films Extrusion

Commercial corn starch composed of 26%–30% amylose and 74%–70% amylopectin with less than 0.5% gluten and 12% moisture content was supplied by Corn Products Brazil Ltda. (São Paulo, Brazil). Extruded films were obtained by mixing the corn starch and glycerol in a ratio of 70:30 [37]. The mixture was processed in a single-screw extruder (AX Plastics, São Paulo, Brazil) with a single feed and three heating zones, where temperatures were kept at 80, 95, and 115 °C from the feed zone to the exit of the die, with a screw speed of 30 rpm. Corn starch was extruded in strip form and cooled to room temperature. Then it was placed in a desiccator.

2.2. Plasma Modification

Corn starch substrates were placed on the cathode of a glow discharge reactor operating at 13.56 MHz. The chamber vacuum was set below 8 Pa. Two different surfaces were produced: (i) TPS coated by hexamethyldisiloxane (HMDSO) and (ii) TPS modified by He plasma followed by coating with HMDSO (He/HMDSO). The same cathode self-bias voltage, $V_b = -60$ V, and the same treatment time, 20 min, were used for each treatment with HMDSO, while $V_b = -100$ V for 10 min was used for every treatment with He.

2.3. Contact Angle Measurements

Water contact angle measurements were carried out with a goniometer NRL A-100-00 (Ramé-Hart, Succasunna, NJ, USA). Each measurement consisted of n = 4 Values being acquired and averaged, with the standard deviation assumed as the respective uncertainty of the means. The time evolution of the water droplet (2.5 mL) shape was recorded using video image capture every 15 s for a total time of 150 s.

2.4. Water Vapor Permeation Analysis

Water vapor permeation (WVP) tests were conducted according to ASTM D1653 (2013) with some modifications. Each sample was placed in a Teflon permeation cell, sealing a circular opening with diameter of 34 mm, and then stored at 25 °C in a desiccator. To maintain a 75% relative humidity (RH) gradient across the film, phosphorus pentoxide (0% RH) was placed inside the cell and silica gel was used in the desiccator. The RH inside the cell was always lower than outside, and water vapor transport was determined from the weight gain of the permeation cell. After steady-state conditions were reached (in about 2 h), eight weight measurements were performed at intervals of 30 min from the first to the second hour. After that, the intervals used were 0, 30, 60, 90, 120, 180, 240, 300, and 360 min. In this case, it was not possible to perform the tests for a total time of 24 h, because the starch films cracked. Changes in the weight of the cell were recorded to the nearest 0.0001 g and plotted as a function of time. The slope of each line was calculated by linear regression ($R^2 > 0.99$), and the water vapor transmission rate (*WVTR*) was calculated from the slope of the tangent line ($g \cdot s^{-1}$), divided by the cell area (m^2). After the permeation tests, film thickness was measured, and the *WVP* coefficient ($g \cdot Pa^{-1} \cdot s^{-1} \cdot m^{-1}$) was calculated according to the following equation:

$$WVP = \frac{WVTR \times d}{S(R_1 - R_2)} \tag{1}$$

where S is the saturation vapor pressure of water (Pa) at the test temperature (25 °C); R_1 is the RH in the desiccator; R_2 is the RH in the permeation cell, and d is the film thickness (m). All tests were conducted in triplicate.

2.5. Water Absorption

The water absorption tests were performed based on ASTM D570-98 (2010). However, since the plasma treatments were performed on only one side of the starch films, it was necessary to adapt the standard to the characteristics of the samples used for these tests. Hence, only a 0.8 cm^2 area of the film was placed in contact with a column of distilled water, i.e., the samples were not completely immersed in water. The samples were dried for 24 h in an oven at 50 °C and then cooled to room temperature in a desiccator containing silica gel. After cooling, the samples were weighted and then were arranged in an acrylic holder and fastened one-by-one to small acrylic plates. This was done so that the samples were well secured and there was no leakage of the distilled water. The samples were placed in contact with the column of distilled water for 2 min, so that the structural integrity of the starch films was maintained. Excess water was then removed from the samples with absorbent paper, and the samples were weighted.

According to this protocol, after immersion and weighting, the samples need to be reconditioned for the same time and at the same temperature as before. This should be done

for samples having an appreciable amount of water-soluble ingredients, to determine the mass of soluble material. However, after repackaging, the samples became brittle, as also observed by [8]. Thus, the water absorption rate *WAI* (%) was calculated by the increase of mass during contact with the water column, according to the following equation:

$$WAI = \frac{(m_{wet} - m_{dry})}{m_{wet}} \times 100\% \qquad (2)$$

where m_{wet} is the sample mass after contact with the water column, and m_{dry} is the sample dry mass. For plasma-treated films, the reduction of absorbed water content *AWR* (%) was calculated by the following Equation (3):

$$AWR = \frac{(WAI_{recover} - WAI_{substrate})}{WAI_{substrate}} \times 100\% \qquad (3)$$

where $WAI_{recover}$ (%) and $WAI_{substrate}$ (%) are the water absorption index of a starch film with and without treatment, respectively.

2.6. SEM Imaging

SEM micrographs at 1000× and 5000× magnification of untreated starch film and of the films produced by the different treatments were obtained with a JEOL JSM (model 6460 LV, San Jose, CA, USA) and Inspect S50 operated at 12.5 and 15 kV, respectively. The samples were coated with 25 nm of gold.

2.7. AFM Imaging and Data Processing

2.7.1. AFM Measurements

An AFM 1M Plus (JPK Instruments, Berlin, Germany) was used to obtain images of the samples, working in amplitude-modulation dynamic mode in ambient air. We used a probe NSC14/Al BS (MikroMasch, Berlin, Germany), with nominal resonance frequency and a spring constant of 160 kHz and 5 N/m, respectively. The typical scan sizes were 20 μm (for preliminary inspection) and 5 μm (for high-resolution mapping), with line scan rates of 1 and 2 Hz, respectively. In all cases, the images were 256 × 256 pixels. For each film, four regions were imaged, at the two difference scan sizes mentioned, to ensure a statistically significant sampling of the actual surfaces. In no case were major defects or anomalies of the surfaces found, and the overall look appeared comparable, on each sample, on all acquired images.

2.7.2. Height Distribution Analysis

AFM images were processed using the MountainsMap Premium software trial version 8.4.8872. The most relevant height-distribution parameters were extracted according to ISO 25178-2: 2012 [38], namely root mean square (RMS) S_q, skewness S_{sk}, and kurtosis S_{ku}. Additionally, textural parameters such as furrows and contour lines were obtained and quantitatively analyzed to provide an accurate determination of the general nature of the films' nanotexture. The interpretation of these parameters was based on [24,38,39].

2.7.3. Power Spectrum Density and Fractal Parameters

To evaluate the films spatial complexity, fractal theory was applied, using three fractal parameters: fractal dimension (*FD*), fractal lacunarity (*FL*), and fractal succolarity (*FS*). Before this, we computed the power spectrum density (*PSD*) in accordance with the theory described by Jacobs et al. [40] using the following equation:

$$PSD^{1D}(q_x) = L_x^{-1} \left[\int_{Lx} h(x,y) e^{-iq_x x} dx \right]^2 \qquad (4)$$

where L_x is image pixels number per line; $h(x,y)$ represents the AFM values of relative height, and q_x is the wave vector linked to x coordinate. The average PSD spectra were obtained by linearized graphics using the software WSxM 5.0 [41]. The Hurst coefficient (*H*) was also computed, using the curve slopes of linear fits applied on the average *PSD*. *FD* was obtained from MountainsMap using the box counting method. *FL* was obtained according to the model proposed by Salcedo et al. [42]. For the quantitative assessment of the surface texture homogeneity, according to Matos et al. [21], we calculated the lacunarity coefficient (*β*) using the following equation:

$$L(r) = \alpha \times r^{\beta} \tag{5}$$

where *L(r)* is lacunarity; *α* is a constant, and *r* is the box size. This parameter was obtained from a height matrix extracted from the AFM topographic maps. This same matrix was used to compute *FS*. However, *FS* was obtained using the model proposed by Heitor et al. [43], according to the following equation:

$$FS(T(k), dir) = \frac{\sum_{k=1}^{n} P_0(T(k)) \times PR(T(k), p_c)}{\sum_{k=1}^{n} PR(T(k), p_c)} \tag{6}$$

where *dir* is liquid entry direction; $P_0(T(k))$ is occupation percentage; *T(k)* are boxes of equal size *T(n)*; *PR* is occupation pressure, and p_c is centroid position (x,y). *FS* and *FL* were computed using algorithms developed in R and FORTRAN 77.

2.7.4. Surface Uniformity Analysis

Uniformity measures are useful to characterize the distribution of asperities over the surface. In this respect, we computed two measures. The first one is the Shannon-based topographic entropy (*E*), which was computed following the formula described in ref. [44]:

$$E = \frac{E^{(2)} - E^{(2)}_{\min}}{E^{(2)}_{\max} - E^{(2)}_{\min}} \tag{7}$$

where the factors $E^{(2)}_{\min}$ and $E^{(2)}_{\max}$ enabled working with a normalized measure, being the information-theory entropy:

$$E^{(2)} = -\sum_{i=1}^{N} \sum_{j=1}^{N} p_{ij} \times \log p_{ij} \tag{8}$$

where p_{ij} is the probability that a matrix term h_{ij} provides a contribution to the total uniformity. Complementarily, we computed a measure that considered local information. Borrowing ideas from other scientific fields that use spatial analysis [45–47], we computed the local *RMS* distribution (*LRMS*), as:

$$LRMS(x,y) = \sqrt{\frac{1}{n} \sum_{x,y} h^2_{(x,y)}} \tag{9}$$

where the neighborhood prescribes *n* = 9, indicating that the sum is reached considering each local set encompassing a focal pixel located at (x,y) and its 8 neighbors. Next, to quantify the level of local uniformity, we computed the fraction of outliers (f_{out}) in the *LRMS*(x,y) distribution. We developed codes in the R programming language, to estimate both global and local uniformity.

3. Results and Discussion

3.1. Contact Angle Measurements

To assess the effect of the observed surface roughness on the wetting behavior of the starch films before and after plasma treatment, the water contact angle was measured and is reported in Figure 1. The untreated film showed such a strong wetting that it was not possible to measure the contact angle, since the drop placed on the surface of that sample was completely spread on the surface. Obviously, the pristine extruded corn starch film is very hydrophilic. On the other hand side, both the extruded films coated with HMDSO and treated with He/HMDSO became hydrophobic, showing water contact angles above 110°, higher than the values found for the treatments performed on starch films obtained by casting [18]. The time evolution of the measurements showed stable values, with only a minor trend of decreasing.
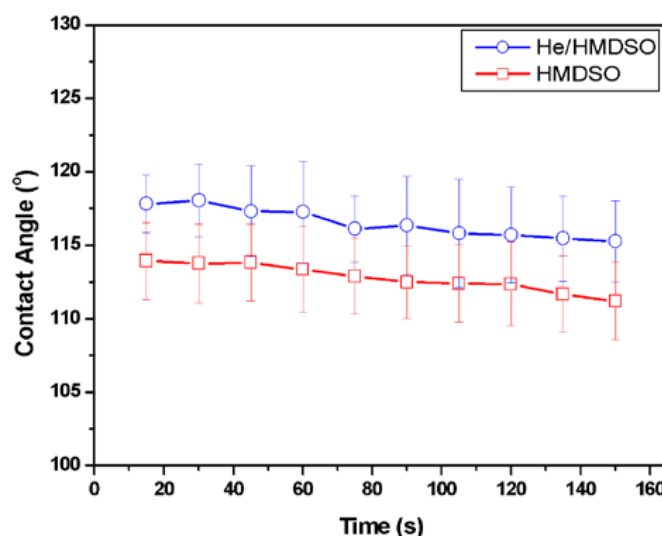

Figure 1. Time evolution of the water contact angle of TPS films after plasma treatments.

3.2. Water Vapor Permeation Analysis

Table 1 shows the *WVP* values of the treated and untreated starch films (average and standard deviation of triplicates). In addition, Table 1 also presents the values of thickness and water vapor transmission of each film.

Table 1. Water vapor permeation of the untreated and treated starch films.

Sample	Thickness (mm)	WVTR ($\times 10^{-3}$ g·s^{-1}·m^{-2})	WVP ($\times 10^{-10}$ g·Pa^{-1}·s^{-1}·m^{-1})
untreated	1.30 ± 0.08	2.11 ± 0.38	8.64 ± 1.47
HMDSO	1.10 ± 0.09	2.45 ± 0.16	8.49 ± 0.12
He/HMDSO	1.41 ± 0.26	1.23 ± 0.67	9.74 ± 1.16

The *WVP* values for both untreated and treated films were very similar. Obviously, in respect of this film functionality, the plasma had neither significant matter-subtractive ('cleaning') effect on the surfaces, nor matter-additive effect due to coating (for HDMSO treatments). Additionally, we also conclude that the vacuum that is operated in the treatment chamber did not have any effect, which is in agreement with the results reported in Mali et al. [48] for corn starch films produced by casting. It should be noticed that the *WVP* values obtained here are one order of magnitude lower than those obtained by Rodríguez-Castellanos et al. [49] for extruded sorghum starch films.

The permeation of gases and vapors through intermolecular spaces is expected to occur in three stages: (i) the sorption and solubilization of the permeant on the material surface, (ii) the diffusion of the permeant through the material, because of the concentration gradient action, and (iii) the desorption and evaporation of the permeate on the other side of the material [1]. According to Al-Hassan and Norziah [50] and Garcia et al. [51], permeation to water vapor also depends on several factors, such as the degree of crystallinity, the mobility of the polymer chains, and the interaction between the functional groups of the polymers and the gases (or vapors) in the amorphous phase. When the degree of crystallinity increases, the *WVP* of the starch films decreases, since permeation occurs through the amorphous zones of the film [48,52]. Other factors, such as temperature, humidity, thickness, and plasticizer concentration also influence the *WVP* of films [53], wherein the hydrophilic character of glycerol favors the absorption and desorption of water molecules [54]. According to Mali et al. [1], films with low permeability can be used for packaging dehydrated products. In the case of starch films, which are very permeable, they can be used as packaging for fresh vegetables.

3.3. Water Absorption

The values of water absorption rate obtained in water absorption tests were: 4.10 ± 0.66 (untreated), 0.86 ± 0.12 (HMDSO), and 1.02 ± 0.12 (He/HMDSO), % by weight. The values of the reduction of absorbed water content were: 78.82 ± 3.91 (HMDSO) and 74.81 ± 3.25 (He/HMDSO), % by weight. Obviously, there was a significant reduction of the absorbed water content of the plasma-treated starch films. Due to their hygroscopic nature, untreated starch films are more prone to moisture and water absorption, since water molecules can act as a natural plasticizer [55,56]. According to Matsuda et al. [57], this action of water as a plasticizer weakens the internal hydrogen bonds between the polymer chains, resulting in an increase in the molecular space. Glycerol, which is a hydrophilic plasticizer, interacts with the starch chains, also increasing molecular mobility, causing an increase in the flexibility and hydrophilicity of the films [58].

The water absorption results indicated that He/HMDSO and HMDSO plasma treatments probably formed a physical barrier against water absorption. According to the literature [15–17], treatments performed with HMDSO plasma can be used to form hydrophobic layers and produce barrier films for food packaging and pharmaceutical applications.

3.4. SEM Analysis

For the untreated extruded corn starch film, it was not possible to obtain a representative SEM micrograph without cracking. Figure 2 shows the TPS micrographs after plasma treatments. It was possible to observe a plasticizing effect of the glycerol in the extruded TPS, besides some residues of starch grains and a relatively rough surface. Observing Figure 2c,d, it can be seen that the treatment performed with He followed by HMDSO plasma was more homogeneous, with smaller HMDSO granules when compared to the coating done only with HMDSO plasma, this result being similar to that obtained for the treatments made in thermoplastic starch films obtained by casting [18].
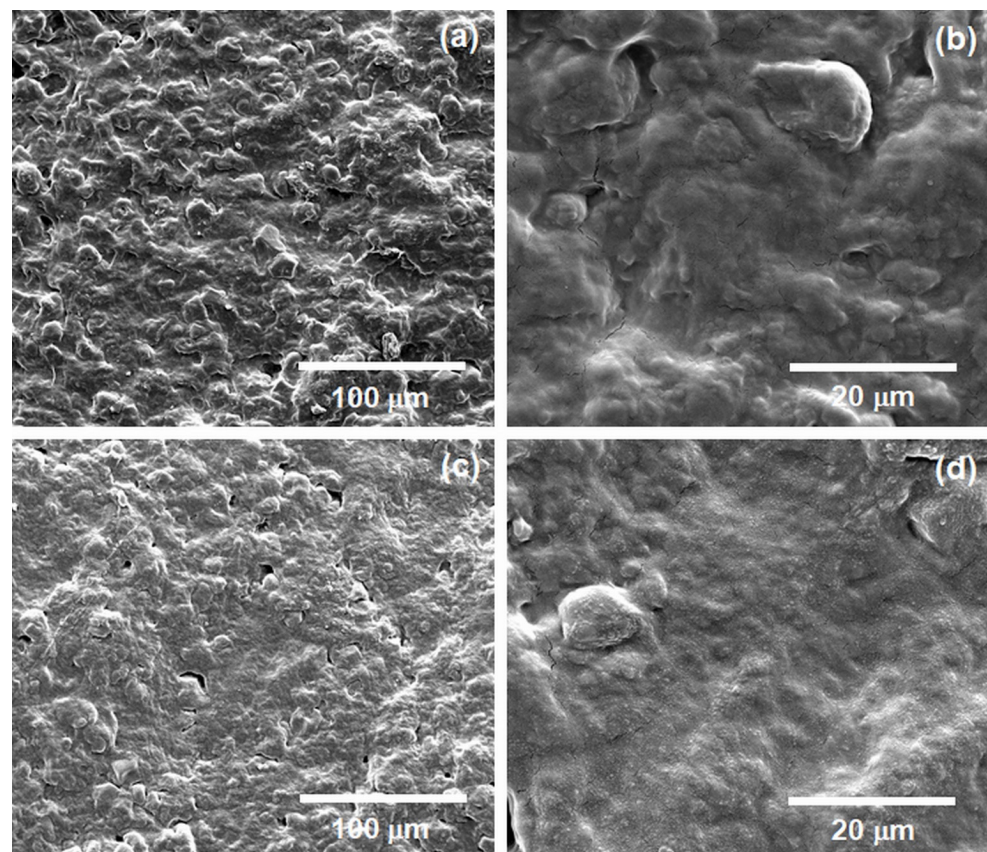
Figure 2. Surface morphology, obtained by SEM, of the TPS after plasma treatment: (**a**) HMDSO, 1000×; (**b**) HMDSO, 5000×; (**c**) He/HMDSO, 1000×; e (**d**) He/HMDSO, 5000×.

3.5. AFM Measurements

3.5.1. Evaluation of Morphology

The main morphological characteristics of the starch films extruded in three different conditions can be observed by looking at three representative surface topography images obtained by AFM, as selected and presented in Figure 3. In the first column, 2D top-view topography projections are reported, whereas in the second column, the same height maps are rendered in a 3D perspective. For all images, the brightness and contrast have equalized to the color palettes, meaning that the lowest height level is in all cases the darkest one, while the highest level is the brightest one. Given the different ranges of values used in the three cases (∼460 nm for Figure 3a,b, ∼490 nm for Figure 2c,d, and ∼260 nm for Figure 3e,f), obviously the untreated starch film (Figure 3a,b) was the roughest of all. This is probably due to the presence of starch granules non-coalesced during the extrusion process. This result is different from those obtained by [59,60] but similar to those for films developed with other plasticizers by [61,62]. For the film coated with HDMSO (Figure 3c,d), a heterogeneous surface like that of the untreated film was observed, composed of grains of HDMSO forming thick structures on the surface. However, the starch film modified by He plasma followed by coating with HMDSO (He/HDMSO) (Figure 3e,f) had the smoothest surface, with smaller HMDSO grains compared to the coating done with HMDSO-only plasma. This particular result was similar to that observed by treating thermoplastic starch films obtained by casting [18].
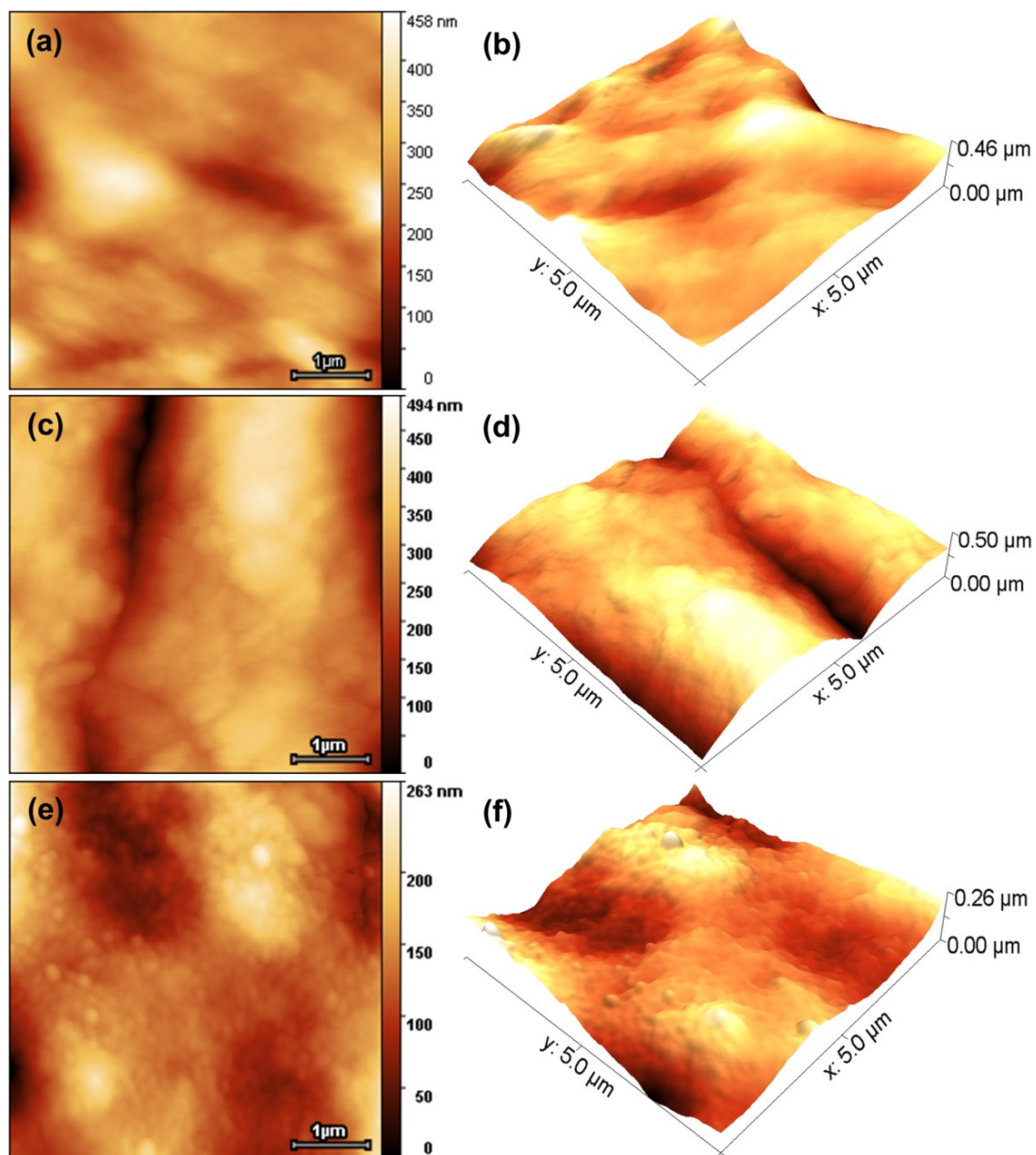
Figure 3. AFM relevant images of the untreated and treated TPS thin films: (**a**,**b**) untreated, (**c**,**d**) HDMSO-treated, and (**e**,**f**) He/HDMSO-treated.

The morphological changes due to treatments were more clearly analyzed through the quantitative evaluation of the height distributions, resulting in some figures showing a statistically significant difference ($p < 0.05$); see Table 2. According to the previously observed qualitative effect of apparent surface roughness, the He/HDMSO films resulted in the lowest value of S_q, while the untreated films had the highest S_q. However, all films exhibited roughness higher than that observed by [63] ($Sq \sim 8$ nm). However, HDMSO treatment led to a smoother surface, showing a decrease in roughness of about 30% as compared to the untreated films, while He/HDMSO treatment induced the appearance of modified small starch granules on the surface and a more homogeneous surface, with $S_q = (37 \pm 8)$ nm.

Table 2. Height surface parameters of the untreated and treated starch films, according to ISO 25178-2:2012, (n = 4).

Parameter	Unit	Untreated	HDMSO	He/HDMSO
S_q	[nm]	97 ± 15	60 ± 13	37 ± 8
S_{sk}	[-]	0.0 ± 0.1	-0.4 ± 0.1	0.1 ± 0.3
S_{ku}	[-]	3.5 ± 0.7	3.7 ± 0.5	3.2 ± 0.3
S_p	[nm]	389 ± 15	238 ± 36	131 ± 23
S_v	[nm]	316 ± 15	233 ± 43	123 ± 33
S_z	[nm]	706 ± 0	471 ± 77	254 ± 45
S_a	[nm]	76 ± 15	46 ± 10	29 ± 6

Additionally, maximum peak height (S_p), maximum valley depth (S_v), and maximum height of surface ($S_z = S_p + S_v$) decreased after the modification by He plasma followed by coating with HMDSO. This decrease in roughness suggests the formation of a more homogeneous surface due to the plasma treatment and can be associated with the organization of the apolar HMDSO groups on the film surface. Another hint of the morphological changes associated with plasma treatment is the behavior of the third central moment of the height distributions, namely skewness S_{sk}, which describes deviation from symmetry; compared to the value around zero for the untreated film, S_{sk} had a negative value (i.e., a predominance of valleys versus mountains) for the HDMSO-coated film, while it was larger than zero (i.e., a predominance of mountains versus valleys) for the He/HDMSO film. As for the fourth central moment, namely kurtosis (S_{ku})—which describes peakedness—it also decreased with He/HDMSO treatment, while staying higher than three (i.e., leptokurtic behavior) for all films. The reduction of all other roughness parameters can explain the increase in the contact angle of the He/HMDSO-coated surface as compared to the HMDSO-coated one, as also reported by Bastos et al. [6].

3.5.2. Evaluation of Nanotexture

Figure 4 shows application of qualitative rendering tools carried out onto the AFM topographic maps using MountainsMap Premium software trial version 8.4.8872. These tools allow for more detailed insight into the surface microtexture of the films, like the contour lines of the surface elevation height, the appearance of furrows, and the weight of feature directions present in the images.

The contour lines revealed connected regions likely associated with the agglomeration of non-coalesced starch granules. These regions appeared to a lesser extent in Figure 4g (He/HDMSO film), as compared to Figure 4d (HDMSO film) and Figure 4a (untreated film), which was already expected based on the former analysis of height distributions. In addition, the furrows maps and the respective quantitative figures extracted (see Table 3) revealed that HDMSO film (Figure 4b) and untreated film (Figure 4e) had deeper channels than the He/HDMSO film (Figure 4h), suggesting the lower wettability of the latter. In fact, HDMSO and untreated films exhibited the highest values for maximum furrow depth (*MFD*) and average furrow depth (*AFD*) (Table 3), which is in accordance with the spatial roughness pattern. However, the average furrow density (*AFDsty*) increased significantly for He/HDMSO film compared to untreated and HDMSO films, because He/HDMSO film exhibited abundant smaller starch granules in the surface, which promoted a greater distribution of nano-furrows along the surface (Figure 4h).
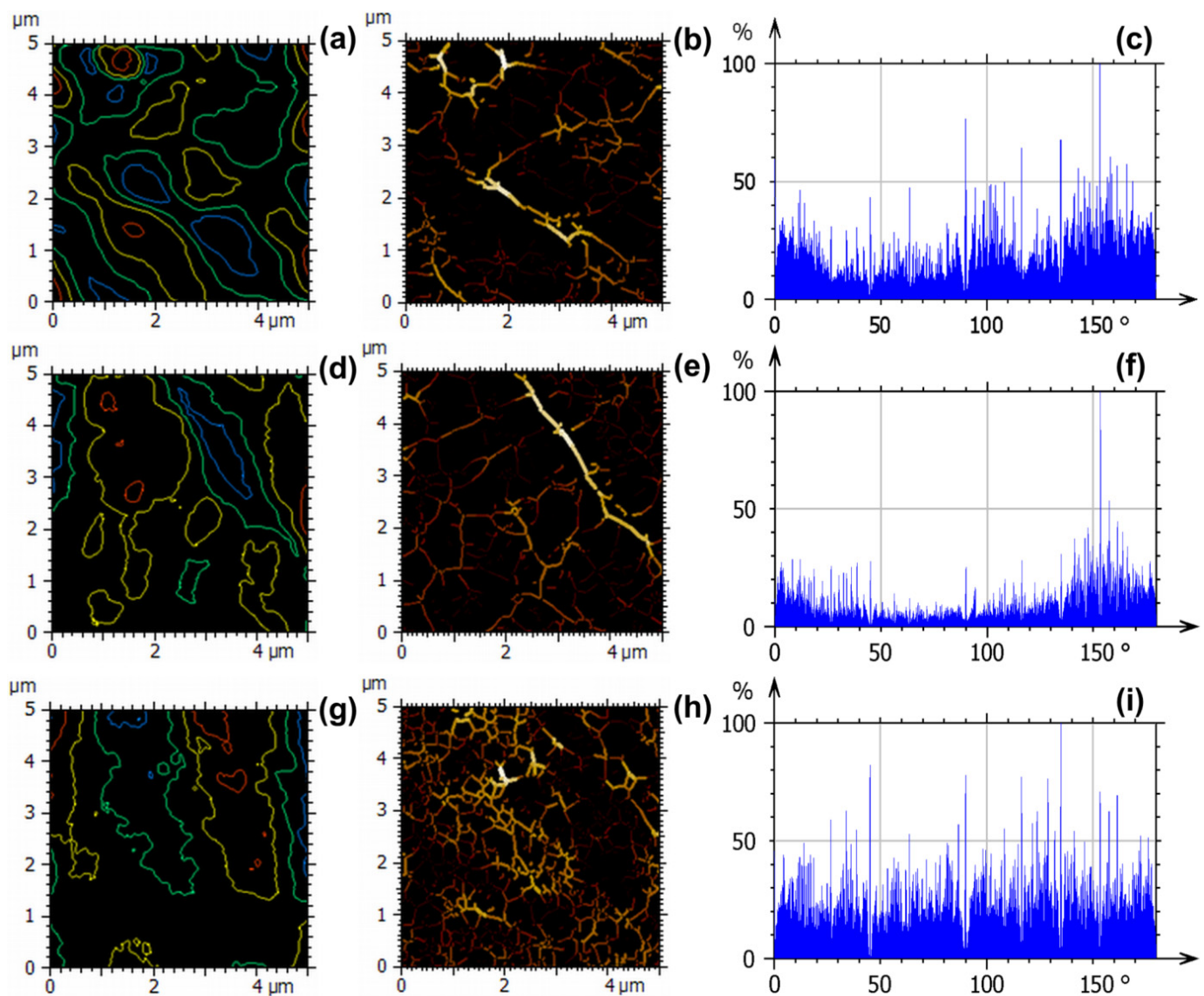
Figure 4. Contour lines (**a,d,g**), furrows (**b,e,h**), and dominant texture directions (**c,f,i**) of (**a–c**) untreated, (**d–f**) HDMSO-treated, and (**g–i**) He/HDMSO-treated TPS films.

Table 3. Texture parameters of the untreated and treated starch thin films, according to ISO 25178-2:2012.

Parameter	Unit	Untreated	HDMSO	He/HDMSO
MFD	[nm]	193 ± 54	140 ± 14	53 ± 6
AFD	[nm]	71 ± 18	47 ± 7	21 ± 3
AFDsty	[cm/cm^2]	25,040 ± 992	26,883 ± 537	38,408 ± 1383
TI *	[%]	35 ± 12	49 ± 21	48 ± 15
S$_{al}$ *	[nm]	0.47 ± 0.03	0.47 ± 0.04	0.48 ± 0.05
S$_{tr}$	[-]	0.6 ± 0.2	0.3 ± 0.1	0.28 ± 0.1
S$_{td}$ *	[°]	165 ± 9	134 ± 39	117 ± 14
1st direction *	[°]	144 ± 9	117 ± 30	101 ± 19
2nd direction	[°]	159 ± 3	74 ± 38	113 ± 39
3rd direction *	[°]	121 ± 64	83 ± 47	119 ± 23

* Samples without significant difference after one-way ANOVA ($p < 0.05$).

The results of this analysis revealed a similar nanotexture for all starch films. This was observed for texture isotropy (*TI*), autocorrelation length (S_{al}), and texture direction (S_{td}). Therefore, we can conclude that, although the roughness of the films was different, the physical properties and the spatial frequency components remained unchanged. However, the texture–aspect ratio (S_{tr}) decreased from the untreated film to the He/HDMSO film, showing that, although the surfaces exhibited a similar texture, there was a tendency to obtain a more anisotropic texture (i.e., S_{tr} tending to 0) [21] with treatment. Again, although there was no significant difference, S_{td} also seemed to confirm this tendency towards more a anisotropic texture, because the angles decreased from the untreated film to the He/HDMSO film. This can be an important characteristic, since more isotropic textures (with the second dominant direction deviating more from the first one, as is the case for the HDMSO film; see Table 3) are likely to make the surfaces more resistant to random-oriented stress. However, since the films exhibited a similar texture, this suggests that the film structure was not significantly altered by the surface treatment, resulting only in a decreased roughness mainly for the He/HDMSO treatment, indicating that the main surface features of the starch films were preserved. This can explain the large decrease in water permeation, even though no change in water vapor (humidity) permeation was observed. All changes induced by the plasma were local changes that mainly modified the chemistry of the starch substrate without any major change in the starch molecules' configuration.

3.5.3. Advanced Fractal and Power Spectral Density Analysis of the Nanotexture

The spatial complexity of the film surfaces was evaluated using mathematical tools from fractal theory. *FL* curves are shown in Figure 5a–c, which revealed that the starch films had fractal behavior, as the lacunarity decreased according to the increase in the box size. Likewise, the average spectra of the *PSD* are displayed in Figure 5d–f, which show that all films exhibited similar dominant frequency signals.

The values found for *FD*, *FS*, *β*, and *H* are shown in Table 4. For all parameters, there was no significant difference among the differently treated starch films. This behavior is consistent with film texture isotropy. Basically, the treated and untreated starch films exhibited low spatial complexity (*FD* < 2.5) and similar dominant wavelength, in addition to uniformly similar textures, because *H* and *β* showed no significant difference, respectively. Furthermore, the films exhibited similar near-ideal surface percolation (*FS*~0.5) [43]. When *FS* is close to ideal, there is a 50% probability that fluids can penetrate films through the upper bands and reach the lower bands, showing a balance in starch film percolation [21,64]. Therefore, these results revealed that, while the surface roughness decreased due to the surface treatment, the surface texture was not significantly affected, which is in accordance with texture direction parameter S_{td}.

Table 4. Advanced fractal parameters of the untreated and treated starch films.

Parameter	Untreated	HDMSO	He/HDMSO
FD *	2.11 ± 0.03	2.13 ± 0.01	2.12 ± 0.01
FS *	0.49 ± 0.02	0.46 ± 0.01	0. 50 ± 0.02
|*β*| *	0.05 ± 0.03	0.06 ± 0.05	0.09 ± 0.05
H *	0.990 ± 0.111	0.996 ± 0.004	0.985 ± 0.090

* Samples without significant difference after one-way ANOVA ($p < 0.05$).
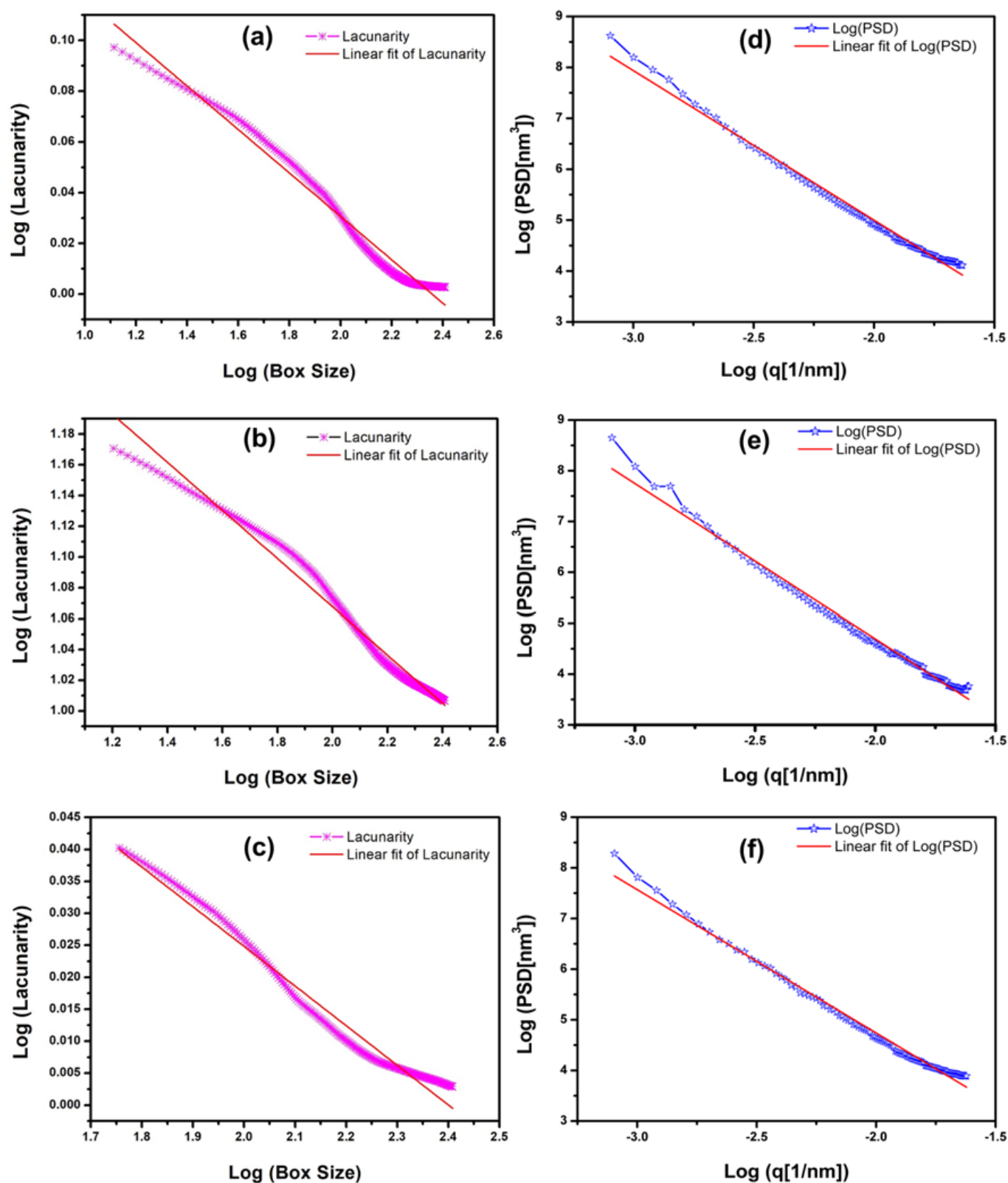
Figure 5. Log–log plots of (**a**–**c**) lacunarity versus box size and (**d**–**f**) *PSD* versus *q*, including linear regressions that allowed us to estimate the lacunarity coefficient ($|\beta|$) and the Hurst coefficient (*H*) of (**a**–**d**) untreated, (**b**–**e**) HDMSO-treated, and (**c**–**f**) He/HDMSO-treated TPS films.

3.5.4. Uniformity Analysis

The results are reported in Table 5. It appears that all samples exhibited high values of Shannon-based topographic entropy (E~1) [65] associated with the height matrix $z(x,y)$ of the AFM images. This means that all untreated and treated starch films had high global uniformity of the arrangement of surface asperities. This is in line with the small fractions of outliers ($f_{out} << 1$) in the $LRMS(x,y)$ distribution, indicating that, on a neighbor-based scale, there is also a high level of uniformity of the roughness arrangement on the surface.

Table 5. Normalized entropy (E) and fraction of outliers (f_{out}) in the $LRMS(x,y)$ of the untreated and treated starch films.

Parameter	Untreated	HMDSO	He/HMDSO
E *	0.97 ± 0.02	0.96 ± 0.02	0.98 ± 0.00
f_{out} *	0.017 ± 0.017	0.025 ± 0.017	0.010 ± 0.003

* Samples without significant difference after one-way ANOVA ($p < 0.05$).

Taken together, the high magnitude of the information-theory-based measure E~1 and the low magnitude of the statistical parameter $f_{out} << 1$ provide evidence that the topographic organization of the asperities remained robust with different surface treatments. This is in accordance with the previously discussed statistical robustness of the texture isotropy (TI), autocorrelation length (S_{al}), and texture direction (S_{td}), despite the changes in the roughness of the films.

4. Conclusions

The He/HMDSO combined treatment on the extruded corn starch films resulted in a surface with a more homogeneous coating and smaller granules compared to the coating with HMDSO-only plasma. The contact angle measurements demonstrated that the treatments with HMDSO and He/HMDSO plasma destroyed the hydrophilicity of the films obtained by extrusion, converting their wetting response to a hydrophobic character, with water contact angle values higher than 110°. The roughness created by He plasma was not effective in increasing the water contact angle of the modified surface. The values of water vapor permeation obtained for both untreated and plasma-treated films were very similar and all high, indicating that, even after plasma treatment, the starch films have potential for use in packaging fresh vegetables. The water absorption assays showed that a significant reduction in the absorbed water content occurred for the plasma-treated starch films, indicating that the treatments with both He/HMDSO and HMDSO probably formed a barrier to water absorption of approximately 80%. The plasma coating with HMDSO appeared on average to be more suitable to make the surface hydrophobic, acting as a physical barrier to water and allowing permeation to water vapor, even if there was no substantial difference with the combined treatment (He/HMDSO) film. Thus, using HMDSO plasma coating alone would optimize the preparation of the desired surfaces, saving time and energy and reducing the cost, since He is a relatively expensive gas. The changes observed in the film morphology according to the type of surface modification were consistent with the observed behavior of the measured physical properties, mainly in relation to the roughness, flatness, and asymmetry of the height distribution. However, the texture of the films did not present significant differences, as texture directions, spatial complexity, dominant spatial frequency, homogeneous void distribution, and surface percolation were all similar for all films. Therefore, we did not confirm our null hypothesis, and we conclude that these coatings did not show a direct correlation between morphology and barrier properties.

References

1. Mali, S.; Grossmann, M.V.E.; Yamashita, F. Filmes de Amido: Produção, Propriedades e Potencial de Utilização. *Semin. Ciênc. Agrárias* **2010**, *31*, 137–156. [CrossRef]
2. Martins, S.; Barros, M.M.; da Costa Pereira, P.S.; Bastos, D.C. Use of Manufacture Residue of Fluidized-Bed Catalyst-Cracking Catalyzers as Flame Retardant in Recycled High Density Polyethylene. *J. Mater. Res. Technol.* **2019**, *8*, 2386–2394. [CrossRef]
3. Gerardo, C.F.; França, S.C.A.; Santos, S.F.; Bastos, D.C.A. A Study of Recycled High-Density Polyethylene with Mica Addition: Influence of Mica Particle Size on Wetting Behavior, Morphological, Physical, and Chemical Properties. *Int. J. Dev. Res.* **2020**, *10*, 37223–37228. [CrossRef]
4. Marengo, V.A.; Vercelheze, A.E.S.; Mali, S. Compósitos Biodegradáveis de Amido de Mandioca e Resíduos Da Agroindústria. *Quim. Nova* **2013**, *36*, 680–685. [CrossRef]
5. Souza, R.C.R.; Andrade, C.T. Investigação Dos Processos de Gelatinização e Extrusão de Amido de Milho. *Polímeros* **2000**, *10*, 24–30. [CrossRef]
6. Bastos, D.C.; Santos, A.E.F.; da Fonseca, M.D.; Simão, R.A. Inducing Surface Hydrophobization on Cornstarch Film by SF6 and HMDSO Plasma Treatment. *Carbohydr. Polym.* **2013**, *91*, 675–681. [CrossRef] [PubMed]
7. Santos, A.E.F.; Bastos, D.C.; da Silva, M.L.V.J.; Thiré, R.M.S.M.; Simão, R.A. Chemical Analysis of a Cornstarch Film Surface Modified by SF6 Plasma Treatment. *Carbohydr. Polym.* **2012**, *87*, 2217–2222. [CrossRef]
8. Thiré, R.M.S.M.; Simão, R.A.; Araújo, P.J.G.; Achete, C.A.; Andrade, C.T. Redução Da Hidrofilicidade de Filmes Biodegradáveis à Base de Amido Por Meio de Polimerização Por Plasma. *Polímeros* **2004**, *14*, 57–62. [CrossRef]
9. Yan, Q.; Hou, H.; Guo, P.; Dong, H. Effects of Extrusion and Glycerol Content on Properties of Oxidized and Acetylated Corn Starch-Based Films. *Carbohydr. Polym.* **2012**, *87*, 707–712. [CrossRef]
10. Hulleman, S.H.; Kalisvaart, M.; Janssen, F.H.; Feil, H.; Vliegenthart, J.F. Origins of B-Type Crystallinity in Glycerol-Plasticised, Compression-Moulded Potato Starches. *Carbohydr. Polym.* **1999**, *39*, 351–360. [CrossRef]
11. Ren, Y.; Wang, C.; Qiu, Y. Aging of Surface Properties of Ultra High Modulus Polyethylene Fibers Treated with He/O_2 Atmospheric Pressure Plasma Jet. *Surf. Coatings Technol.* **2008**, *202*, 2670–2676. [CrossRef]
12. Zanini, S.; Massini, P.; Mietta, M.; Grimoldi, E.; Riccardi, C. Plasma Treatments of PET Meshes for Fuel–Water Separation Applications. *J. Colloid Interface Sci.* **2008**, *322*, 566–571. [CrossRef]
13. Bogaerts, A.; Neyts, E.; Gijbels, R.; van der Mullen, J. Gas Discharge Plasmas and Their Applications. *Spectrochim. Acta Part B Spectrosc.* **2002**, *57*, 609–658. [CrossRef]
14. Chan, C.-M.; Ko, T.-M.; Hiraoka, H. Polymer Surface Modification by Plasmas and Photons. *Surf. Sci. Rep.* **1996**, *24*, 1–54. [CrossRef]
15. Choudhury, A.J.; Barve, S.A.; Chutia, J.; Pal, A.R.; Kishore, R.; Jagannath; Pande, M.; Patil, D.S. RF-PACVD of Water Repellent and Protective HMDSO Coatings on Bell Metal Surfaces: Correlation between Discharge Parameters and Film Properties. *Appl. Surf. Sci.* **2011**, *257*, 8469–8477. [CrossRef]
16. García-Luis, A.; Corengia, P.; González-Santamaría, D.; Brizuela, M.; Braceras, I.; Briz, N.; Azpiroz, P.; Bellido-González, V.; Powell, S. Synthesis and Characterization of Plasma-Polymerized HMDSO Films Using an Ion Gun Inverse Magnetron Source. *Plasma Process. Polym.* **2007**, *4*, S766–S770. [CrossRef]
17. Morent, R.; De Geyter, N.; Van Vlierberghe, S.; Dubruel, P.; Leys, C.; Schacht, E. Organic–Inorganic Behaviour of HMDSO Films Plasma-Polymerized at Atmospheric Pressure. *Surf. Coatings Technol.* **2009**, *203*, 1366–1372. [CrossRef]
18. de Albuquerque, M.D.F.; Bastos, D.C.; Simão, R.A. Surface Modification of Starch Films by Plasma. *Macromol. Symp.* **2014**, *343*, 96–101. [CrossRef]

19. Fattahi, M.; Nezafat, N.B.; Ţălu, Ş.; Solaymani, S.; Ghoranneviss, M.; Elahi, S.M.; Shafiekhani, A.; Rezaee, S. Topographic Characterization of Zirconia-Based Ceramics by Atomic Force Microscopy: A Case Study on Different Laser Irradiations. *J. Alloys Compd.* **2020**, *831*, 154763. [CrossRef]

20. Ţălu, Ş.; Achour, A.; Solaymani, S.; Nikpasand, K.; Dalouji, V.; Sari, A.; Rezaee, S.; Nezafat, N.B. Micromorphology Analysis of TiO$_2$ Thin Films by Atomic Force Microscopy Images: The Influence of Postannealing. *Microsc. Res. Technol.* **2020**, *83*, 457–463. [CrossRef]

21. Matos, R.S.; Ramos, G.Q.; da Fonseca Filho, H.D.; Ţălu, Ş. Advanced Micromorphology Study of Microbial Films Grown on Kefir Loaded with Açaí extract. *Micron* **2020**, *137*, 102912. [CrossRef] [PubMed]

22. Rashid, D.; Stach, S.; Ţălu, Ş.; Sobola, D.; Méndez-Albores, A.; Córdova, G.T.; Grmela, L. Stereometric Analysis of Effects of Heat Stressing on Micromorphology of Si Single Crystals. *Silicon* **2019**, *11*, 2945–2959. [CrossRef]

23. Barcelay, Y.R.; Moreira, J.A.G.; Almeida, A.J.M.; Brito, W.R.; Matos, R.S.; da Fonseca Filho, H.D. Nanoscale Stereometric Evaluation of BiZn$_{0.5}$Ti$_{0.5}$O$_3$ Thin Films Grown by RF Magnetron Sputtering. *Mater. Lett.* **2020**, *279*, 128477. [CrossRef]

24. Matos, R.S.; Pinto, E.P.; Ramos, G.Q.; de Albuquerque, F.M.D.; Filho, F.H.D. Stereometric Characterization of Kefir Microbial Films Associated with Maytenus Rigida Extract. *Microsc. Res. Technol.* **2020**, *83*, 1401–1410. [CrossRef]

25. Arman, A.; Ţălu, Ş.; Luna, C.; Ahmadpourian, A.; Naseri, M.; Molamohammadi, M. Micromorphology Characterization of Copper Thin Films by AFM and Fractal Analysis. *J. Mater. Sci. Mater. Electron.* **2015**, *26*, 9630–9639. [CrossRef]

26. Senthilkumar, M.; Sahoo, N.K.; Thakur, S.; Tokas, R.B. Characterization of Microroughness Parameters in Gadolinium Oxide Thin Films: A Study Based on Extended Power Spectral Density Analyses. *Appl. Surf. Sci.* **2005**, *252*, 1608–1619. [CrossRef]

27. Ţălu, Ş.; Stach, S.; Valedbagi, S.; Elahi, S.M.; Bavadi, R. Surface Morphology of Titanium Nitride Thin Films Synthesized by DC Reactive Magnetron Sputtering. *Mater. Sci.* **2015**, *33*, 137–143. [CrossRef]

28. Ţălu, Ş.; Bramowicz, M.; Kulesza, S.; Shafiekhani, A.; Ghaderi, A.; Mashayekhi, F.; Solaymani, S. Microstructure and Tribological Properties of FeNPs@a-C:H Films by Micromorphology Analysis and Fractal Geometry. *Ind. Eng. Chem. Res.* **2015**, *54*, 8212–8218. [CrossRef]

29. Silva, M.R.P.; Matos, R.S.; Estevam, C.S.; Santos, S.B.; da Silva, F.M.A.; Sousa, I.G.P.P.; Filho, F.H.D.; Almeida, L.E. Structural Evaluation of Polymeric Microbial Films Grown on Kefir Loaded with Maytenus Rigida Extract. *Microsc. Res. Technol.* **2021**, *84*, 627–638. [CrossRef]

30. Shakoury, R.; Rezaee, S.; Mwema, F.; Luna, C.; Ghosh, K.; Jurečka, S.; Ţălu, Ş.; Arman, A.; Grayeli Korpi, A. Multifractal and Optical Bandgap Characterization of Ta$_2$O$_5$ Thin Films Deposited by Electron Gun Method. *Opt. Quantum Electron.* **2020**, *52*, 95. [CrossRef]

31. Yadav, R.P.; Kumar, M.; Mittal, A.K.; Pandey, A.C. Fractal and Multifractal Characteristics of Swift Heavy Ion Induced Self-Affine Nanostructured BaF$_2$ Thin Film Surfaces. *Chaos Interdiscip. J. Nonlinear Sci.* **2015**, *25*, 083115. [CrossRef] [PubMed]

32. Sapota, W.; Szczepanik, P.; Stach, S.; Wróbel, Z. Fractal and Multifractal Analyses of the Porosity Degree of Ceramics Used in Biomedicine. *Adv. Sci. Eng. Med.* **2020**, *12*, 450–456. [CrossRef]

33. Almeida, P.A.; Pinto, E.P.; Filho, H.D.F.; Matos, R.S. Distribution of Microorganisms on Surface of Kefir Biofilms Associated with Açaí Extract Distribution of Microorganisms on Surface of Kefir Biofilms Associated with Açaí Extract. *Sci. Amaz.* **2019**, *8*, C10–C18.

34. Ferraro, M.A.N.; Pinto, E.P.; Matos, R.S. Study of the Superficial Distribution of Microorganisms in Kefir Biofilms Prepared with Cupuaçu Juice. *J. Bioenergy Food Sci.* **2020**, *7*, 2732019. [CrossRef]

35. de Oliveira, L.M.; Matos, R.S.; Campelo, P.H.; Sanches, E.A.; Filho, F.H.D. Evaluation of the Nanoscale Surface Applied to Biodegradable Nanoparticles Containing Allium Sativum Essential Oil. *Mater. Lett.* **2020**, *275*, 128111. [CrossRef]

36. Pinto, E.; Tavares, W.; Matos, R.; Ferreira, A.; Menezes, R.; Costa, M.; Souza, T.; Ferreira, I.; Sousa, F.; Zamora, R. Influence of Low and High Glycerol Concentrations on Wettability and Flexibility of Chitosan Biofilms. *Quim. Nova* **2018**, *41*, 1109–1116. [CrossRef]

37. Corradini, E.; Lotti, C.; de Medeiros, E.S.; Carvalho, A.J.F.; Curvelo, A.A.S.; Mattoso, L.H.C. Estudo Comparativo de Amidos Termoplásticos Derivados Do Milho Com Diferentes Teores de Amilose. *Polímeros* **2005**, *15*, 268–273. [CrossRef]

38. Blateyron, F. *Characterisation of Areal Surface Texture*; Leach, R., Ed.; Springer: Berlin/Heidelberg, Germany, 2013; Volume 9783642364, ISBN 978-3-642-36457-0.

39. Franco, L.A.; Sinatora, A. 3D Surface Parameters (ISO 25178-2): Actual Meaning of S_{pk} and Its Relationship to V_{mp}. *Precis. Eng.* **2015**, *40*, 106–111. [CrossRef]

40. Jacobs, T.D.B.; Junge, T.; Pastewka, L. Quantitative Characterization of Surface Topography Using Spectral Analysis. *Surf. Topogr. Metrol. Prop.* **2017**, *5*, 013001. [CrossRef]

41. Horcas, I.; Fernández, R.; Gómez-Rodríguez, J.M.; Colchero, J.; Gómez-Herrero, J.; Baro, A.M. WSXM: A Software for Scanning Probe Microscopy and a Tool for Nanotechnology. *Rev. Sci. Instrum.* **2007**, *78*, 013705. [CrossRef]

42. Salcedo, M.O.C.; Zamora, R.R.M.; Carvalho, J.C.T. Study Fractal Leaf Surface of the Plant Species Copaifera Sp. Using the Microscope Atomic-Force-AFM. *Revista ECIPerú* **2016**, *13*, 10–16. [CrossRef]

43. Heitor, R.; De Melo, C.; De Melo, R.H.C.; Conci, A. Succolarity: Defining a Method to Calculate This Fractal Measure. In Proceedings of the 15th International Conference on Systems, Signals and Image Processing, Bratislava, Slovakia, 25–28 June 2008. [CrossRef]

44. Nosonovsky, M. Entropy in Tribology: In the Search for Applications. *Entropy* **2010**, *12*, 1345–1390. [CrossRef]

45. Woodcock, C.E.; Strahler, A.H. The Factor of Scale in Remote Sensing. *Remote Sens. Environ.* **1987**, *21*, 311–332. [CrossRef]

46. Aja-Fernandez, S.; Estepar, R.S.J.; Alberola-Lopez, C.; Westin, C.-F. Image Quality Assessment Based on Local Variance. In Proceedings of the 2006 International Conference of the IEEE Engineering in Medicine and Biology Society, New York, NY, USA, 15 December 2016; pp. 4815–4818.

47. Drăguţ, L.; Eisank, C.; Strasser, T. Local Variance for Multi-Scale Analysis in Geomorphometry. *Geomorphology* **2011**, *130*, 162–172. [CrossRef]

48. Mali, S.; Grossmann, M.V.E.; García, M.A.; Martino, M.N.; Zaritzky, N.E. Barrier, Mechanical and Optical Properties of Plasticized Yam Starch Films. *Carbohydr. Polym.* **2004**, *56*, 129–135. [CrossRef]

49. Rodríguez-Castellanos, W.; Martínez-Bustos, F.; Jiménez-Arévalo, O.; González-Núñez, R.; Galicia-García, T. Functional Properties of Extruded and Tubular Films of Sorghum Starch-Based Glycerol and Yucca Schidigera Extract. *Ind. Crops Prod.* **2013**, *44*, 405–412. [CrossRef]

50. Al-Hassan, A.A.; Norziah, M.H. Starch–Gelatin Edible Films: Water Vapor Permeability and Mechanical Properties as Affected by Plasticizers. *Food Hydrocoll.* **2012**, *26*, 108–117. [CrossRef]

51. Garcia, M.A.; Martino, M.N.; Zaritzky, N.E. Lipid Addition to Improve Barrier Properties of Edible Starch-Based Films and Coatings. *J. Food Sci.* **2000**, *65*, 941–944. [CrossRef]

52. Galdeano, M.C.; Grossmann, M.V.E.; Mali, S.; Bello-Perez, L.A.; Garcia, M.A.; Zamudio-Flores, P.B. Effects of Production Process and Plasticizers on Stability of Films and Sheets of Oat Starch. *Mater. Sci. Eng. C* **2009**, *29*, 492–498. [CrossRef]

53. Bertuzzi, M.A.; Castro Vidaurre, E.F.; Armada, M.; Gottifredi, J.C. Water Vapor Permeability of Edible Starch Based Films. *J. Food Eng.* **2007**, *80*, 972–978. [CrossRef]

54. Alves, V.D.; Mali, S.; Beléia, A.; Grossmann, M.V.E. Effect of Glycerol and Amylose Enrichment on Cassava Starch Film Properties. *J. Food Eng.* **2007**, *78*, 941–946. [CrossRef]

55. Yew, G.H.; Yusof, M.A.M.; Ishak, M.Z.A.; Ishiaku, U.S. Water Absorption and Enzymatic Degradation of Poly(Lactic Acid)/Rice Starch Composites. *Polym. Degrad. Stab.* **2005**, *90*, 488–500. [CrossRef]

56. Preechawong, D.; Peesan, M.; Supaphol, P.; Rujiravanit, R. Characterization of Starch/Poly(ε-Caprolactone) Hybrid Foams. *Polym. Test.* **2004**, *23*, 651–657. [CrossRef]

57. Matsuda, D.K.M.; Verceheze, A.E.S.; Carvalho, G.M.; Yamashita, F.; Mali, S. Baked Foams of Cassava Starch and Organically Modified Nanoclays. *Ind. Crops Prod.* **2013**, *44*, 705–711. [CrossRef]

58. Shimazu, A.A.; Mali, S.; Grossmann, M.V.E. Efeitos Plastificante e Antiplastificante Do Glicerol e Do Sorbitol Em Filmes Biodegradáveis de Amido de Mandioca. *Semin. Ciênc. Agrárias* **2007**, *28*, 79. [CrossRef]

59. Mendes, J.F.; Paschoalin, R.; Carmona, V.B.; Sena Neto, A.R.; Marques, A.C.P.; Marconcini, J.M.; Mattoso, L.H.C.; Medeiros, E.S.; Oliveira, J.E. Biodegradable Polymer Blends Based on Corn Starch and Thermoplastic Chitosan Processed by Extrusion. *Carbohydr. Polym.* **2016**, *137*, 452–458. [CrossRef]

60. Kuutti, L.; Peltonen, J.; Myllärinen, P.; Teleman, O.; Forssell, P. AFM in Studies of Thermoplastic Starches during Ageing. *Carbohydr. Polym.* **1998**, *37*, 7–12. [CrossRef]

61. Pushpadass, H.A.; Marx, D.B.; Hanna, M.A. Effects of Extrusion Temperature and Plasticizers on the Physical and Functional Properties of Starch Films. *Starch—Stärke* **2008**, *60*, 527–538. [CrossRef]

62. Thiré, R.M.S.; Simão, R.A.; Andrade, C.T. High Resolution Imaging of the Microstructure of Maize Starch Films. *Carbohydr. Polym.* **2003**, *54*, 149–158. [CrossRef]

63. Rindlav-Westling, Å.; Gatenholm, P. Surface Composition and Morphology of Starch, Amylose, and Amylopectin Films. *Biomacromolecules* **2003**, *4*, 166–172. [CrossRef]

64. Ito, R.M.; de Souza, C.C.; Gandarilla, A.M.D.; de Oliveira, L.M.; Brito, W.R.; Sanches, E.A.; Matos, R.S.; da Fonseca Filho, H.D. Micromorphology and Microtexture Evaluation of Poly(o-Ethoxyaniline) Films Using Atomic Force Microscopy and Fractal Analysis. *J. Polym. Res.* **2020**, *27*, 299. [CrossRef]

65. Matos, R.S.; Lopes, G.A.C.; Ferreira, N.S.; Pinto, E.P.; Carvalho, J.C.T.; Figueiredo, S.S.; Oliveira, A.F.; Zamora, R.R.M. Superficial Characterization of Kefir Biofilms Associated with Açaí and Cupuaçu Extracts. *Arab. J. Sci. Eng.* **2018**, *43*, 3371–3379. [CrossRef]